THE HYDROGEN EXOSPHERIC DENSITY PROFILE MEASURED WITH ASPERA-3/NPD

A. GALLI[1,*], P. WURZ[1], H. LAMMER[2], H. I. M. LICHTENEGGER[2], R. LUNDIN[3],

Institut für Weltraumforschung, Österreichische Akademie der Wissenschaften, A-8042 Graz, Austria
[3]*Swedish Institute of Space Physics, Box 812, SE-981 28 Kiruna, Sweden*
(*Author for correspondence: E-mail: galli@space.unibe.ch)

(Received 4 April 2006; Accepted in final form 25 October 2006)

Abstract. We have evaluated the Lyman-α limb emission from the exospheric hydrogen of Mars measured by the neutral particle detector of the ASPERA-3 instrument on Mars Express in 2004 at low solar activity (solar activity index = 42, $F_{10.7} = 100$). We derive estimates for the hydrogen exobase density, $n_H = 10^{10}$ m^{-3}, and for the apparent temperature, $T > 600$ K. We conclude that the limb emission measurement is dominated by a hydrogen component that is considerably hotter than the bulk temperature at the exobase. The derived values for the exosphere density and temperature are compared with similar measurements done by the Mariner space probes in the 1969. The values found with Mars Express and Mariner data are brought in a broader context of exosphere models including the possibility of having two hydrogen components in the Martian exosphere. The present observation of the Martian hydrogen exosphere is the first one at high altitudes during low solar activity, and shows that for low solar activity exospheric densities are not higher than for high solar activity.

Keywords: Martian exosphere, UV airglow measurements

1. Introduction

The physical properties of the Martian exosphere determine atmospheric loss rates, which are in turn necessary to understand the water inventory evolution of the planet (Lammer *et al.*, 2003). The thermal escape rate, for example, depends directly upon exospheric temperatures. The ASPERA-3 experiment on board the Mars Express spacecraft has been designed to study the interaction of the solar wind with the upper atmosphere (Barabash *et al.*, 2004) by measuring ions, electrons and energetic neutral atoms (ENAs). It was not designed to study the neutral exosphere directly, but the density and temperature of the hydrogen exosphere are the most important parameters that affect the production of ions and ENAs in the near-Mars space (Holmström *et al.*, 2002).

Unfortunately, there are still no *in situ* data available from the Martian hydrogen exosphere. All temperature and density values have been derived either from airglow measurements of the Lyman-α emission of neutral hydrogen or from aerobraking data (Lichtenegger *et al.*, this issue). The two Viking landers (Nier and McElroy, 1977) have performed mass spectrometer measurements below 200 km altitude,

Space Science Reviews (2006) 126: 447–467
DOI: 10.1007/s11214-006-9089-7

but it has been questioned if the measured temperatures of carbon oxides, nitrogen and argon apply to the exospheric hydrogen, too.

The first work to derive the temperature and the exobase density of the hydrogen corona was done by Anderson and Hord (1971), based on Mariner 6 and 7 Lyman-α airglow measurements at high solar activity (Barth *et al.*, 1971, 1972). Assuming one single temperature for the hydrogen exosphere they derived $T = 350$ K and $n_{\mathrm{H}} = 3 \times 10^{10}$ m^{-3} at 250 km above the surface. Mariner 9 airglow measurements confirmed this temperature (Barth *et al.*, 1972). On the other hand, temperatures derived from mass spectrometer or aerobraking data (186 K and 145 K in the case of the Viking landers, 220 to 230 K for Mars Global Surveyor (Bougher *et al.*, 2000)) are considerably lower. Recent CO_2 dayglow measurements done with SPICAM (Leblanc *et al.*, 2006) for altitudes below 200 km also yield a temperature of only 200 K. In analogy to Venus, where the exospheric hydrogen density profile has been explained (Anderson, 1976; Bertaux *et al.*, 1978) by the presence of a cool bulk component and a tenuous hot population of atoms that have been heated up in photodissociation and dissociative recombination processes, the same approach is proposed by Lichtenegger *et al*. (this issue) for the Martian exosphere to resolve the discrepancy between Lyman-α airglow measurements and *in situ* measurements.

In this work we present a recent Lyman-α airglow measurement performed with the neutral particle detector on Mars Express in 2004 during low solar activity (solar activity index equal to 42). We interpret our measurements with a numerical exosphere model, and we compare the results to the Lyman-α airglow measurements from Mariner 6 and 7 in 1969.

We give a quick overview over the instrument (Section 2) and explain how we calibrated the Lyman-α sensitivity of the neutral particle detector (NPD) that was originally not intended as a UV detector (Section 3). After showing the observation condition for the Lyman-α airglow measurement (Section 4) we introduce the numerical exosphere model and the radiation transport equation that relates the modeled density profile to the measured UV emission (Section 5). We then interpret the UV limb emission: First we assume one single hydrogen component and search for the exosphere model whose temperature and exobase density fits best (Section 6.1). We compare these values for low solar activity to those found from Mariner measurements (Anderson and Hord, 1971) for high solar activity. Finally, we study what constraints the Mariner and Mars Express data put on an exosphere model with two hydrogen components (Section 6.2).

2. Instrumentation

The ASPERA-3 instrument on board the Mars Express spacecraft comprises four different sensors. The ion mass analyser and the electron spectrometer are used to measure local ion and electron densities, and the neutral particle detector (NPD) and the neutral particle imager (NPI) to detect energetic neutral atoms (ENAs)

(Barabash *et al.*, 2004). In the current report we concentrate on one single NPD data set.

The neutral particle detector consists of two identical sensors, NPD1 and NPD2, which are sensitive to ENAs in the energy range of 0.1 to 10 keV using the time-of-flight technique. Each sensor has one start and three stop surfaces, which provide an angular resolution of roughly 30° in azimuthal direction as shown in Figure 4. Although the NPD entrance system has been designed to suppress UV photon count rates the suppression is not complete, and an electronic signal can be triggered on the start and stop surface if the energy of a photon exceeds the ionization potential of the detector surface. The stop surface has an MgO coating with a bandgap of 7.8 eV (Deutscher *et al.*, 1999). Thus, UV radiation at wavelengths below $\lambda = 160$ nm is clearly visible in NPD data:

$$\lambda = hc/E_{\text{crit}}, \quad E_{\text{crit}} = 7.8\,\text{eV} \tag{1}$$

The UV emission of the Martian atmosphere is known (Barth *et al.*, 1972, based on Mariner data) to have no contribution in the wavelength range below 160 nm except from the Lyman-α ($\lambda = 121.6$ nm) line that is caused by resonant scattering of solar UV light on neutral hydrogen atoms. The resonant scattering on helium atoms produces UV emission at even shorter wavelengths ($\lambda = 58.4$ nm), but the disk airglow intensity due to neutral helium has been found to reach only 40 to 70 Rayleigh (R) (Krasnopolsky and Gladstone, 1996, 2005) (1 R$\doteq 10^{10}/(4\pi)\,\text{m}^{-2}\,\text{sr}^{-1}\,\text{s}^{-1}$), which is orders of magnitudes smaller than the hydrogen intensities. Therefore, we can use NPD data to map the neutral hydrogen densities when looking at the Mars exosphere.

3. Calibration of UV Sensitivity

The NPD sensor accumulates signals of incoming ENAs and UV photons in steps of one second by sampling all coincident count events. A start-stop signal pair is regarded as a correlated event, if the time gap between the two signals does not exceed 2048 ns. This time gap allows the detection of ENAs in the energy range between 0.1 and 10 keV. On the other hand, two different photons that by coincidence hit the start and the stop surface within 2048 ns mimic a correlated event as well. ENAs and UV background can be separated only by studying the entire TOF spectrum. This is demonstrated in Figure 1: After integrating the NPD count rates over several minutes a stream of ENAs produces a measurable peak in the TOF spectrum depending on mass and energy of the particles. UV photons, on the other hand, produce a flat noise level, which can appropriately be parameterized by a linear model. Since the NPD detector is only sensitive to hydrogen ENAs above 0.1 keV, corresponding to the first hundred TOF bins, the higher TOF bins of the spectrum can be used to estimate the background level due to UV photons.

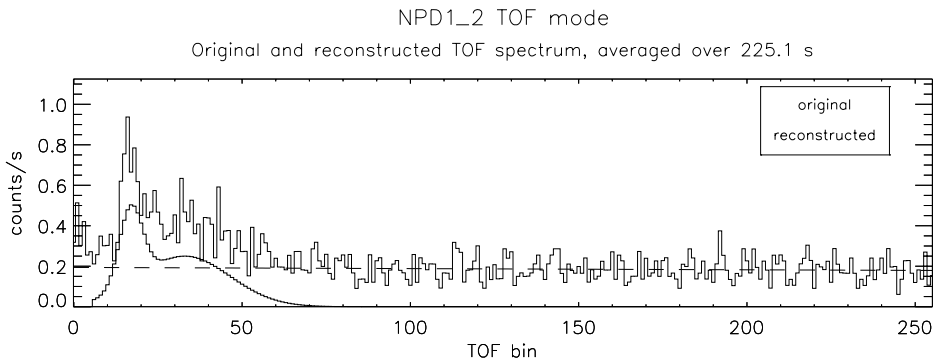

Figure 1. Time-of-flight spectrum measured by NPD1_2 from 12:29 until 12:33 UT on April 25, 2004. The peak between TOF bins 10 and 60 is due to hydrogen ENAs. The flat noise level of 0.2 counts per second is due to coincident photons. According to our calibration (Equation (3)) this level corresponds to a UV flux of 1.17 ± 0.22 kR.

To deduce the UV intensity from the registered background count rate (see Figure 1) the UV sensitivity of the instrument was calibrated using all NPD data from July 2003 to January 2004 during the cruise phase. For these measurements far away from any planetary atmosphere the background reflects only the known UV brightness of the sky. Figure 2 shows our reference UV map. It is a composite picture of UV measurements done by the SWAN experiment on SOHO (NASA, 2006) and gives an average UV intensity in Rayleigh for the year 2004 for all viewing directions. The map includes all non-planetary UV sources: the interstellar gas, single stars and the galactic background. The sensitivity range of the SWAN instrument includes wavelengths from 117 to 180 nm, but the vast majority of the photons belongs to the Lyman-α line of neutral hydrogen at 121.6 nm. The omnidirectional UV background of 300 to 600 R is due to resonant scattering of Lyman-α radiation on interstellar neutral hydrogen. The bright stars in the galactic plane emit UV radiation outside the Lyman-α line, but according to the diffuse sky brightness model of Leinert *et al.* (1998) the UV flux integrated from 140 to 180 nm does not exceed 60 R even in the galactic plane where the stellar UV brightness is highest. Thus, the UV map we have used for calibration (Figure 2) shows in good approximation the Lyman-α photon flux and the NPD instrument registers, at wavelengths below 160 nm, virtually only Lyman-α photons as well. In the following sections, 'UV' and 'Lyman-α' will be used as synonyms by default.

For the subsequent analysis of the Martian limb emission measurement we need to have a relation between the average UV flux inside the field-of-view of an NPD sector and the background count rate that is registered for this viewing direction. The measured background count rate in NPD must be proportional to the probability that two independent UV photons trigger a start and a stop pulse within a small

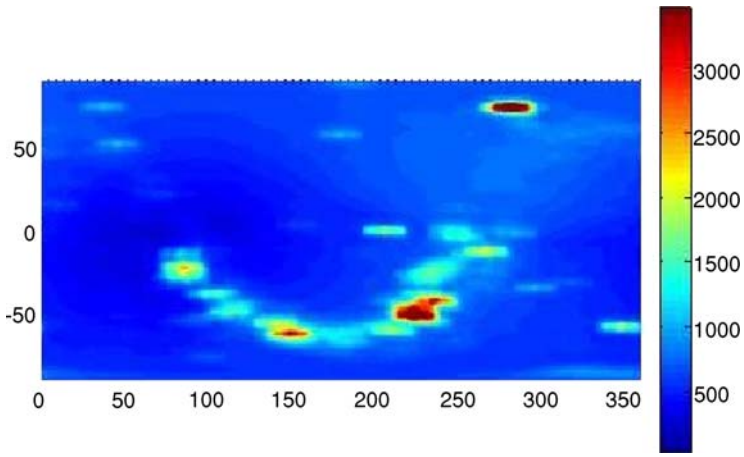

Figure 2. Full-sky image of the UV brightness in the wavelength range $\lambda = 117$ to 180 nm, adapted from measurements made with SWAN on SOHO (NASA, 2006). Coordinates are given in the ecliptic reference frame, the units of the color bar are given in Rayleigh. The dark background is due to the resonant scattering of Lyman-α radiation on interstellar hydrogen atoms, whereas the narrow U-bend shows the galactic plane with its bright UV stars.

time interval. More precisely, we expect the following relationship between the UV intensity I [kR] and the background count rate C [counts s^{-1}]:

$$C = c_1' I^2 + c_0 \text{ or } I = c_1 \sqrt{C - c_0}, \tag{2}$$

with c_0 the dark count rate.

To find the calibration constants c_0 and c_1 we have evaluated all available measurements from the cruise phase. Figure 3 shows the measurements and the least-squares fit curves for two of the six NPD directions, NPD1_1 (triangles) and NPD1_2 (circles). The error bars of the count rates reflect the statistical errors, the uncertainty of the UV intensity is due to possible short time variations of the solar UV irradiance and due to the size of the field-of-view ($4^\circ \times 30^\circ$) that may cover regions of variable UV brightness. This uncertainty is most pronounced for the six data points above 1 kR for which NPD1_1 was directed to the region of α Cen (the dark spot at $\lambda = 240^\circ$, $\beta = -45^\circ$ in Figure 2).

Within the individual error bars Equation (2) describes the UV sensitivity of the instrument. For NPD1_1 a least-squares fit yields for the dark count rate $c_0 = 0$ counts s^{-1} and $c_1 = 2.83 \pm 0.5$ kR $s^{1/2}$. The error bar takes into account the error of the count rates and of the UV intensities. In the following we will only use the calibration constants for NPD1_2 because the UV limb emission measurement was made with this sector. For NPD1_2 we find very similar calibration constants, $c_0 = 0.0037 \pm 0.003$ counts s^{-1} and $c_1 = 2.64 \pm 0.35$ kR $s^{1/2}$. Thus, I and C follow

$$I = (2.64 \pm 0.35)\sqrt{C - 0.0037 \pm 0.003}. \tag{3}$$

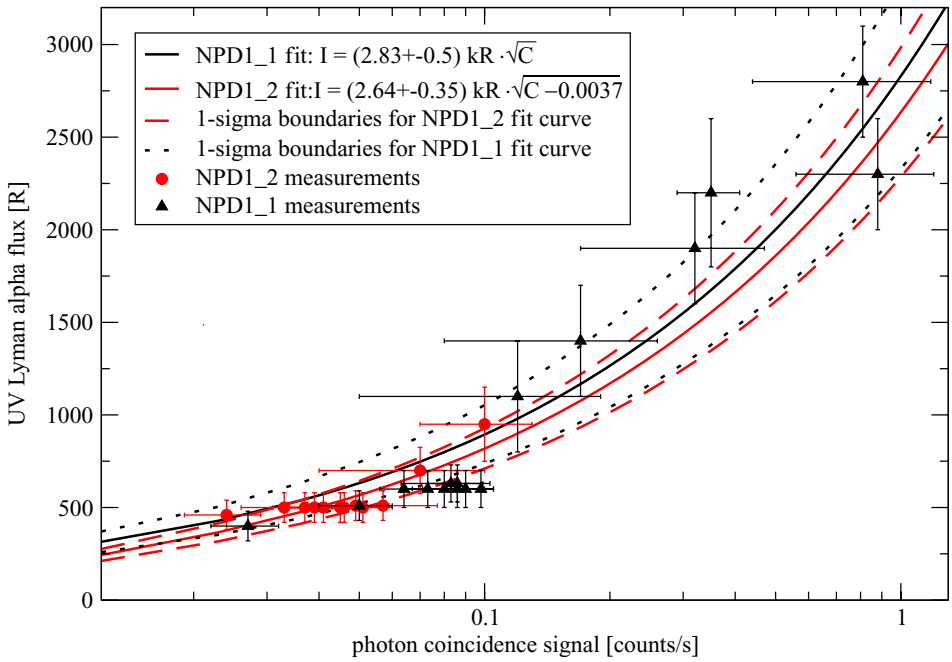

Figure 3. Relationship between UV intensity (*Y*-axis) and registered coincidence count rates (*X*-axis) for the NPD1_1 (triangles) and NPD1_2 (circles) sectors. The data have been obtained during the cruise phase from July 2003 to January 2004, when NPD measured the well known Lyman-α fluxes backscattered from interplanetary hydrogen and from stellar sources (values taken from Figure 2).

4. Limb Emission Measurement

For our study we have chosen the UV signal measured on April 25, 2004, from 12:00 until 13:10 UT, when the NPD field-of-view was directed to the North pole region of the Martian exosphere. The pointing direction of the NPD sensor is fixed with respect to the ecliptic reference frame while Mars with its exosphere slowly moves into the field-of-view of the sensor. This configuration ensures that the Lyman-α background due to the interplanetary hydrogen and the stellar radiation remains constant during the measurement. Figure 4 shows the observation condition for the begin and for the end of the measurement period in a spacecraft-centered view. The solar zenith angle remains constant at 145°.

Figure 5 illustrates the observation geometry: For any given time period the measured UV intensity is proportional to the UV limb emission averaged over the field-of-view and integrated along the line of sight through the Martian exosphere. The so-called tangential height, h_i, is the minimum distance between the line of sight and the Mars surface. For our observation it decreases within 75 minutes from 7250 to 1900 km, whereas the altitude of the spacecraft above the Mars surface,

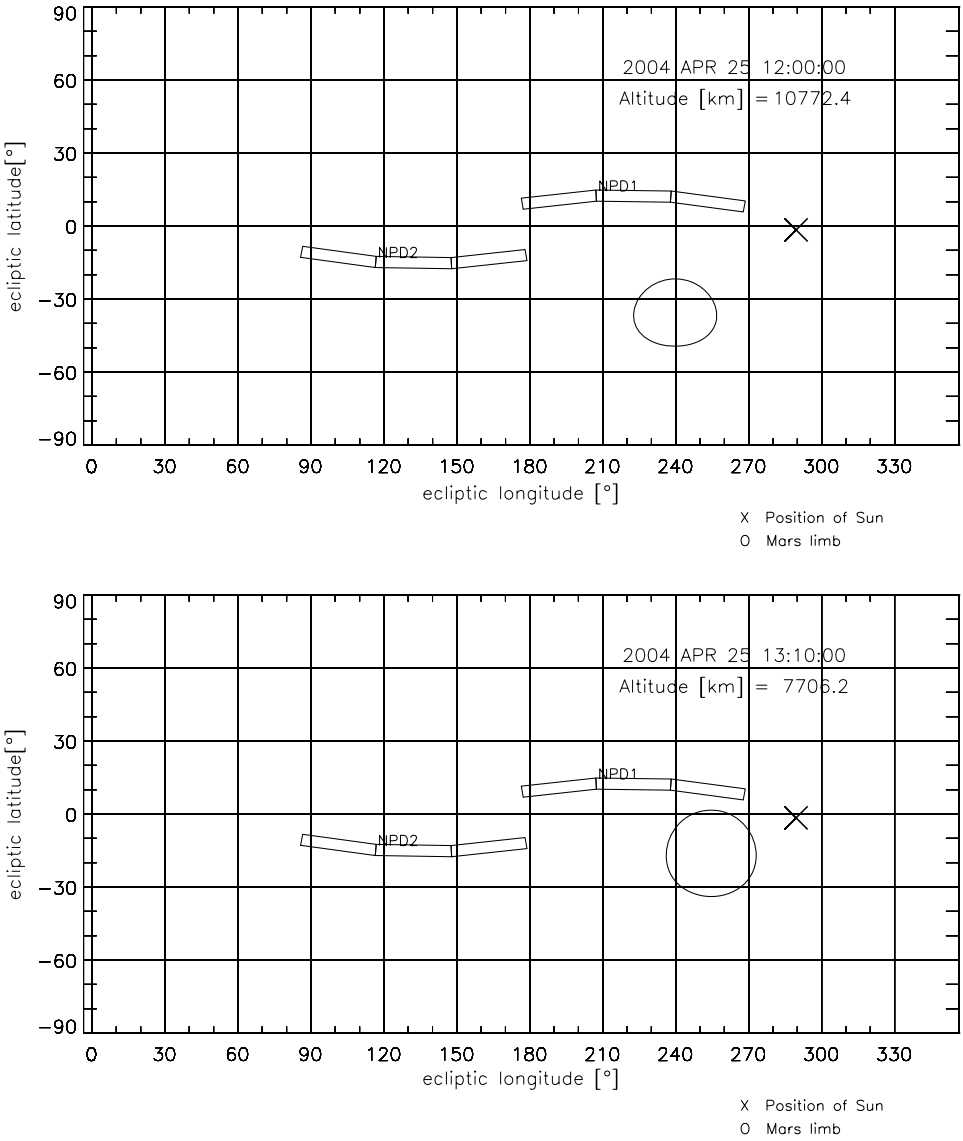

Figure 4. NPD observation directions on April 25, 2004, 12:00 UT (top) and at 13:10 UT (bottom), as seen from the spacecraft. The 2×3 elongated boxes are the fields-of-view of the two NPD sensors with their three angular channels ($4^\circ \times 30^\circ$ each). NPD1_2 is the sector closest to the Sun whose position is indicated with an X.

d_i, decreases from 10,800 to 7,700 km. Before 12:00 UT the instrument was not operating, and a few minutes after 13:15 the line of sight intersected the surface of Mars itself.

We have then divided the observation period into 15 consecutive intervals of 5 minutes duration and retrieved the height of the UV background for each

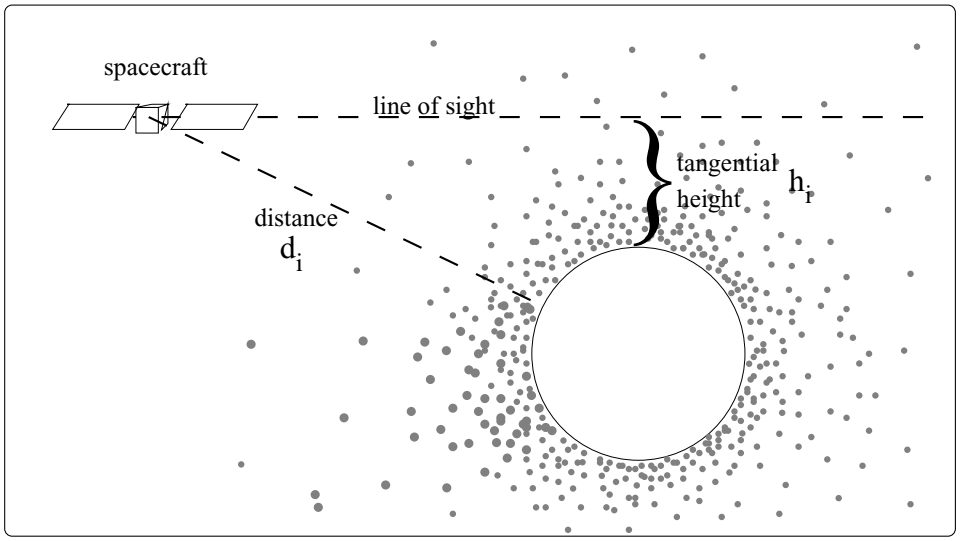

Figure 5. Observation geometry of the limb emission measurement.

measurement. One of the corresponding TOF spectra is shown in Figure 1, in which the dashed line indicates the height of the UV background. These count rates can be converted to Lyman-α intensities (in number of photons per second per steradian per square meter or in kR), since we have calibrated the UV sensitivity of the instrument.

With Equation (3) the 15 different measurements can be plotted as UV fluxes in kR (Figure 6). These fluxes are to be understood as UV emission of the neutral hydrogen integrated along the line of sight through the Martian exosphere. Because the hydrogen particle density is higher close to the planet the limb emission increases as the field-of-view covers deeper layers of the atmosphere. The non-planetary UV background (see Figure 2) has already been subtracted in Figure 6, it is a constant (Equation (10)) because the field-of-view retains its inertial pointing direction over the entire measurement.

5. UV Emission Model and Exosphere Model

If we are to deduce the temperature and the exobase density of the neutral hydrogen from the measured UV fluxes presented in Figure 6, we need two things: first we need a model that yields a hydrogen density profile $n_{\mathrm{H}}(r)$ for a given temperature T and exobase density. Second, we need a radiation transport equation that relates the modeled density profile to a UV emission that can be compared to the measurements.

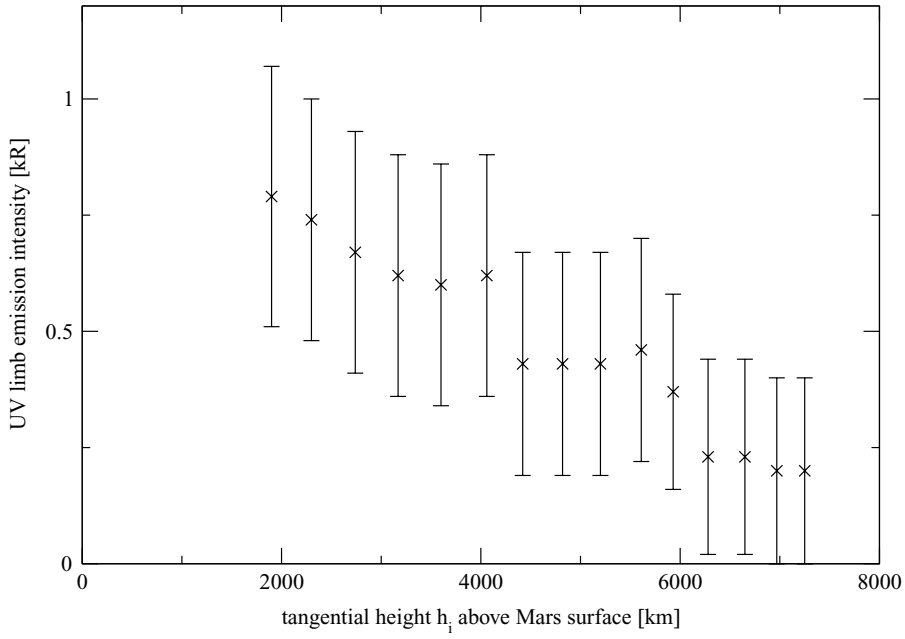

Figure 6. Measured limb emission of the exospheric hydrogen [kR] on April 25, 2004, from 12:00 until 13:15 UT. The error bars reflect the statistical errors, the error of the UV calibration (Equation (3)), and the uncertainty of the subtracted UV background (Equation (10)) from interstellar gas and stellar sources. The values for the height, h_i, are accurate to 300 km, the uncertainty being due to the finite aperture angle of the sensor.

For the exosphere model we assume a spherically symmetric distribution of neutral hydrogen with one single constant temperature. Several components of hydrogen are thought to co-exist in the exosphere (Lichtenegger *et al.*, this issue) but an exosphere with two components will simply be modeled as a linear combination of two different models, each of them with its own exobase density and temperature (see Section 6.2). We assume that the exobase lies at 220 km (Lichtenegger *et al.*, this issue) above the surface, and that the hydrogen atoms are fully thermalized at the exobase. The velocity distribution of particles in the exosphere is of course not Maxwellian. The exospheric density profile results from calculating the trajectories of many particles using a one-dimensional Monte Carlo code (Wurz and Lammer, 2003), for which the exobase density and the temperature are the two free parameters. The differences to a three-dimensional spherically symmetric code are not significant. Keep in mind, however, that a high spatial variability of temperatures and densities has to be expected. According to Holmström (this issue) the hydrogen exobase density may vary as much as an order of magnitude with geographic latitude and solar zenith angle, the lowest exospheric densities in spring 2004 are expected above the North pole.

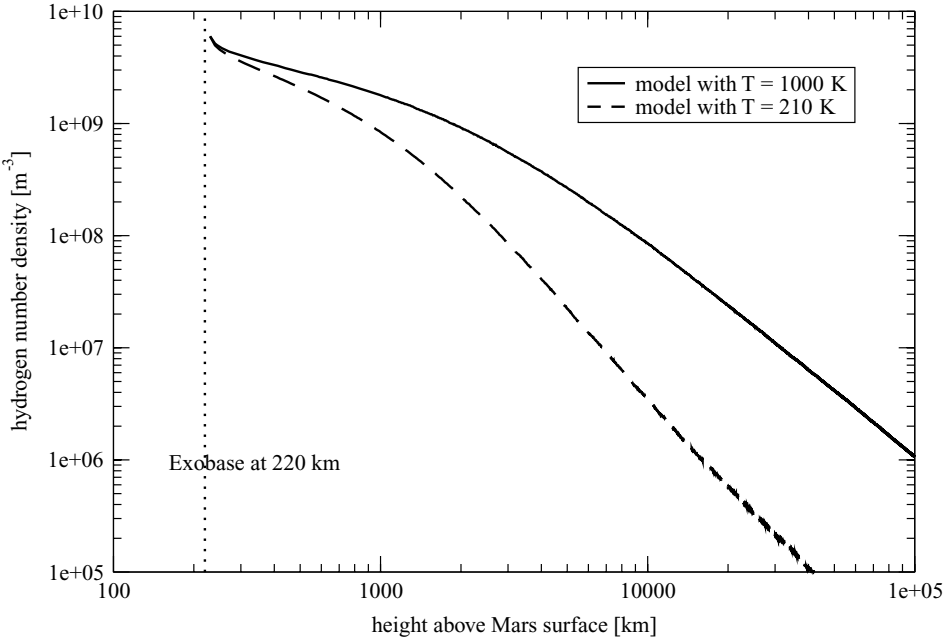

Figure 7. Modeled hydrogen density profiles for two different exospheric temperatures, $T = 210$ K (dashed line) and $T = 1000$ K (solid line). The exobase density is a free parameter and has been set to $n_{\mathrm{H}} = 6 \times 10^9$ m^{-3}.

Two density profiles for different temperatures are presented in Figure 7. Empirically, the density profiles can be expressed as a set of continuous power law functions with differing exponents. For $T = 1000$ K, e.g., we find

$$\begin{aligned}
&1.4 \times 10^{11}\,\mathrm{m}^{-3} r^{-2.92} \quad \text{for } 5.2 < r < 7,\\
&5.6 \times 10^{10}\,\mathrm{m}^{-3}\, r^{-2.47} \quad \text{for } 7 < r < 14.2,\\
&2.9 \times 10^{10}\,\mathrm{m}^{-3}\, r^{-2.22} \quad \text{for } 14.2 < r < 30,\\
&1.8 \times 10^{10}\,\mathrm{m}^{-3}\, r^{-2.07} \quad \text{for } 30 < r < 100,
\end{aligned} \tag{4}$$

with the radial distance $r = (h + R_M)/1000\,\mathrm{km}$.

To compare the modeled exosphere density profile with the UV limb emission measurements, we assume that the UV emission is entirely due to resonant scattering on hydrogen atoms. As discussed above, the Sun is outside the field-of-view and the line of sight is outside Mars eclipse. Moreover, the opacity is small, $\tau \ll 1$, and multiple scattering of UV photons can be disregarded. The opacity, or optical depth along a line of sight through the hydrogen exosphere with the local particle number density $n_{\mathrm{H}}(r)$ calculates to:

$$\tau = \sigma_0 \int_{\mathbf{r}}^{\infty} n_{\mathrm{H}}(r')dr'. \tag{5}$$

The cross-section for resonant scattering amounts to $\sigma_0 = 1.865 \times 10^{-17}$ m^2 (Meier, 1991). As we shall see in Section 6, $\tau < 0.2$ for all tangential heights in Figure 6.

In addition, we re-examine the two data sets from Mariner 6 and 7, presented by Anderson and Hord (1971), with our Monte Carlo model. For these data sets one has to be aware that the last few observations were obtained for lines of sight close to the exobase where the opacity is not negligible any more. For the present work we restrict the analysis to those regions where $\tau < 0.38$.

According to Thomas' (1963) and Bertaux' (1978) work on Lyman-α scattering in the geocorona the following linear relationship between particle density and intensity of UV limb emission is a good approximation under the assumption $\tau \ll 1$, even if the velocity distribution of the scattering particles is non-Maxwellian:

$$I(\mathbf{r}, \Omega) = \frac{f_{Ly-\alpha} \Delta\lambda_D \sqrt{\pi} \sigma_0}{4\pi} \int_{\mathbf{r}}^{\infty} n_{\mathrm{H}}(r') dr' \tag{6}$$

The emission rate factor in front of the integral consists of two natural constants ($\Delta\lambda_D = 0.001647$ nm being the Doppler width of the absorption process) times the central spectral solar Lyman-α irradiance $f_{Ly-\alpha}$ at 121.6 nm. In April 2004 at 1 AU distance the solar activity was low (solar activity index equal to 42) and the Lyman-α line irradiance was measured to be $F_{Ly-\alpha} = 4.22 \times 10^{11}$ cm^{-2} s^{-1} (NASA, 2004). According to the relation derived by Emerich *et al*. (2005) this corresponds to a central spectral irradiance of $f_{Ly-\alpha} = (3.65 \pm 0.10) \times 10^{12}$ cm^{-2} s^{-1} nm^{-1}. Finally, we have to scale the central spectral irradiance with the heliocentric distance of Mars in April 2004 to get the relevant number of Lyman-α photons at 121.6 nm for our UV limb emission measurement,

$$f_{Ly-\alpha} = \left(\frac{1\mathrm{AU}}{1.61\mathrm{AU}}\right)^2 3.65 \times 10^{12}\ \mathrm{s}^{-1}\,\mathrm{cm}^{-2}\ \mathrm{nm}^{-1} = 1.41 \times 10^{12}\ \mathrm{s}^{-1}\,\mathrm{cm}^{-2}\ \mathrm{nm}^{-1}. \tag{7}$$

Thus, we derive from Equation (6) the following relation between particle number densities and the predicted UV emission, I:

$$I(\mathbf{r}, \Omega) = b + k \int_{d}^{\infty} n_{\mathrm{H}}(r) dl, \tag{8}$$

with the emission rate factor k equal to

$$k = (6.1 \pm 0.2) \times 10^{-5}\,\mathrm{s}^{-1}\,\mathrm{sr}^{-1}, \tag{9}$$

where d is the distance of the spacecraft to the planet and l the axis along the NPD line-of-sight. The additive constant b denotes the UV background due to stars and Lyman-α backscattering from interplanetary hydrogen. For the pointing direction

of NPD1_2 ($\lambda_{\rm ecl} = 255^\circ$, $\beta_{\rm ecl} = 10^\circ$) during the observation on April 25, 2004, b reaches according to Figure 2:

$$b = 0.74 \pm 0.1\,\mathrm{kR}. \tag{10}$$

For a given density profile model with $n_{\rm H}(r)$ Equation (8) thus yields the UV emission we would expect in number of photons per seconds per steradian per square meter.

6. Results

To compare the airglow measurements to a modeled density profile, we must evaluate the path integral along the line of sight given in Equation (8). To simplify the notation let us first substitute for the distance of the spacecraft to the planet center $\tilde{d} \doteq d + R_M$, and for the tangential height $\tilde{h} \doteq h + R_M$, where R_M denotes the Mars radius. For the i-th measurement we define the column density as

$$S_{\rm model}(i) \doteq \int_{\tilde{d}_i}^{\infty} n_{\rm H}(r) dl. \tag{11}$$

Since we apply a spherically symmetric exosphere model, this path integral is symmetrical with respect to the radial distance to the center of the planet r, as long as the line of sight does not intersect with the planetary surface or with the eclipse. Thus, we convert the integration variable dl into an integration over dr. Since $\tilde{d}^2 = r^2 + l^2 \pm 2l\sqrt{r^2 - \tilde{h}^2}$

$$S_{\rm model}(i) \doteq \int_{\tilde{d}_i}^{\infty} n_{\rm H}(r) \frac{dl}{dr} dr = \tag{12}$$

$$= \int_{\tilde{d}_i}^{\tilde{h}i} n_{\rm H}(r) \frac{r}{\sqrt{r^2 - \tilde{h_i}^2}} dr + \int_{\infty}^{\tilde{h}_i} n_{\rm H}(r) \frac{r}{\sqrt{r^2 - \tilde{h_i}^2}} dr \tag{13}$$

evaluating the path integral piecewise from $r = \tilde{d}_i \ldots \tilde{h}_i$ and $r = \tilde{h}_i \ldots \infty$. We recognize that

$$\int_{\tilde{d}_i}^{\tilde{h}_i} n_{\rm H}(r) \frac{r}{\sqrt{r^2 - \tilde{h}_i^2}} dr = - \int_{\tilde{h}_i}^{\tilde{d}_i} n_{\rm H}(r) \frac{r}{\sqrt{r^2 - \tilde{h}_i^2}} dr, \tag{14}$$

and we find the following formula for the predicted column density along the line of sight for a given model exosphere:

$$S_{\rm model}(i) = 2 \int_{\tilde{d}_i}^{\tilde{h}_i} n_{\rm H}(r) \frac{r}{\sqrt{r^2 - \tilde{h}_i^2}} dr + \int_{\infty}^{\tilde{d}_i} n_{\rm H}(r) \frac{r}{\sqrt{r^2 - \tilde{h}_i^2}} dr. \tag{15}$$

Because all heights $h_i < 10^4$ km, the second integral in Equation (15) can be approximated as:

$$\int_{10^5\,\mathrm{km}}^{\tilde{d}_i} n_{\mathrm{H}}(r)\frac{r}{\sqrt{r^2-\tilde{h}_i^2}}dr + \int_{\infty}^{10^5\,\mathrm{km}} n_{\mathrm{H}}(r)dr, \tag{16}$$

and since $n_{\mathrm{H}}(r) \sim 1/r^2$ for $r \gg 10^4$ km for any temperature, we can safely ignore the second term in expression 16, and we finally have:

$$S_{\mathrm{model}}(i) = 2\int_{\tilde{d}_i}^{\tilde{h}_i} n_{\mathrm{H}}(r)\frac{r}{\sqrt{r^2-\tilde{h}_i^2}}dr + \int_{10^5\,\mathrm{km}}^{\tilde{d}_i} n_{\mathrm{H}}(r)\frac{r}{\sqrt{r^2-\tilde{h}_i^2}}dr. \tag{17}$$

Equation (17) can be analytically integrated, since the model density profile $n_{\mathrm{H}}(r)$ can be expressed as a series of power law functions (see Equation (4)). We now search for the set of model parameters (temperature and exobase density) whose density profile $n_{\mathrm{H}}(r)$ minimizes the merit function

$$\chi^2 = \sum_{i=1}^{15}(S_{\mathrm{obs}}(i) - S_{\mathrm{model}}(i))^2/\sigma_{\mathrm{obs}}^2(i), \tag{18}$$

where $S_{\mathrm{model}}(i)$ is given by Equation (17), and S_{obs} with the corresponding standard deviation σ_{obs} is the integrated column density deduced from the i-th Lyman-α limb emission measurement according to Equation (8):

$$S_{\mathrm{obs}}(i) = \frac{I(i) - b}{k}. \tag{19}$$

To minimize the merit function in Equation (18) we first optimize for the exobase density for a given temperature, then the χ^2-deviations of the different model temperatures are compared to each other.

This is illustrated in Figure 8. Obviously, χ^2 for $T = 180$ K is much higher than for $T = 1000$ K, even with an optimized exobase density.

6.1. One Single Hydrogen Component

Several components of hydrogen with different temperatures are thought to co-exist in the Martian exosphere (see Section 1) but our measurement uncertainties urge us to test the one-component approach first. The derived values for the exospheric density and for the temperature will be dominated by the hotter hydrogen components because our observations are restricted to the upper exosphere (see the tangential heights in Figure 6). In Section 6.2 we will show the constraints the UV airglow measurements put on a two-component model. Let us first assume that there is only one component of neutral hydrogen with a temperature T and an exobase density $n_{\mathrm{H}}(r_{\mathrm{exo}})$ at 220 km above the surface. If we minimize the

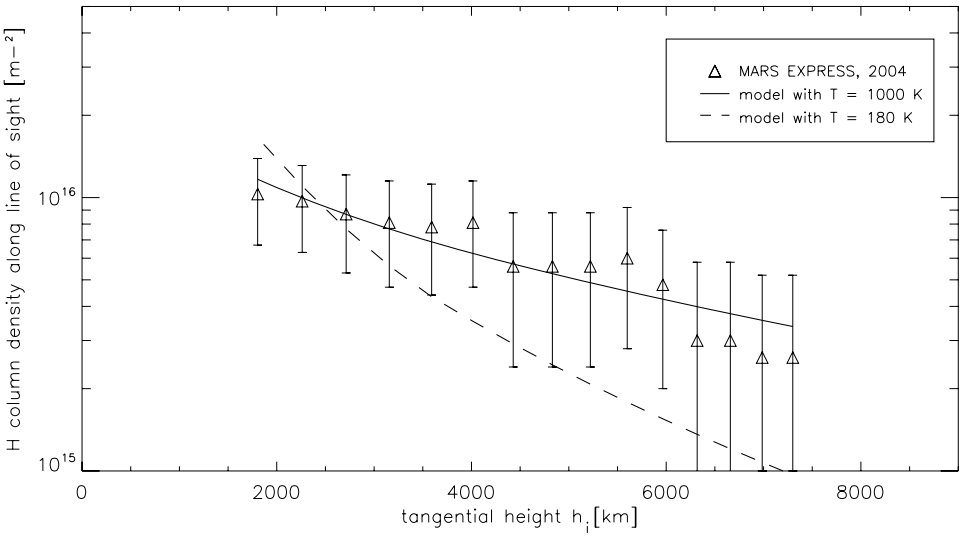

Figure 8. One-component models for a cool and for a hot hydrogen exosphere fitted to the NPD observations (triangles). The exobase densities have been chosen to minimize the χ^2-statistics: For $T = 180$ K we fit $n_{\rm H}(r_{\rm exo}) = 7.6 \times 10^{10}\,{\rm m}^{-3}$ (dashed line), for $T = 1000$ K, on the other hand, we find only $n_{\rm H}(r_{\rm exo}) = 6.4 \times 10^{9}\,{\rm m}^{-3}$ (solid line).

merit function (Equation (18)) we derive the following 1-σ boundaries for the exospheric hydrogen:

$$T = 1000\,^{+\infty}_{-400}\ {\rm K}, \tag{20}$$

$$n_{\rm H}(r_{\rm exo}) = 6.4\,^{+4.0}_{-0.6} \times 10^{9}\,{\rm m}^{-3}, \tag{21}$$

Note that the upper bound of the temperature estimate is ill constrained: An exospheric model with a deliberately high temperature provides almost as good a fit to the data as one with $T = 1000$ K. This is partly due to the large error bars of our measurement (see Figure 6); the other reason is that the modeled density profile does not change its slope substantially for temperatures above 1000 K. For $T \to \infty$, $n_{\rm H}(r)$ in Equation (4) converges to $n_{\rm H}(r) \sim r^{-2}$. Physically, of course, even the most energetic exospheric component cannot exceed a few 10^3 K (Lichtenegger *et al.*, this issue).

To re-evaluate the Mariner 6 and 7 measurements from 1969 published by Anderson and Hord (1971) we adopt their original values for the emission rate factor ($k = 8 \times 10^{-5}\,{\rm sr}^{-1}\,{\rm s}^{-1}$) and the UV background ($b = 300$ R) but we restrict ourselves to the data points above 3000 km where the optical depth of the exosphere can be neglected. We then compare the Mariner measurements to our exosphere

model and we find, according to the same merit function (Equation (18)) and with the same statistical criteria:

$$T = 350\,^{+100}_{-50}\ \mathrm{K}, \tag{22}$$

$$n_{\mathrm{H}}(r_{\mathrm{exo}}) = 7.1\,^{+0.7}_{-1.6} \times 10^{10}\,\mathrm{m}^{-3}, \tag{23}$$

for Mariner 6. For Mariner 7, which approached Mars one week later, we find:

$$T = 425 \pm 50\ \mathrm{K} \tag{24}$$

$$n_{\mathrm{H}}(r_{\mathrm{exo}}) = 3.4\,^{+1.6}_{-0.5} \times 10^{10}\,\mathrm{m}^{-3}. \tag{25}$$

These results are plotted in Figure 9 and summarized in Table I. Anderson and Hord (1971) found, based on a Chamberlain exosphere (Chamberlain, 1963) model, $T = 350 \pm 100$ K and $n_{\mathrm{H}}(r_{\mathrm{exo}}) = (3.0 \pm 1.0) \times 10^{10}\,\mathrm{m}^{-3}$ for Mariner 6 and $n_{\mathrm{H}}(r_{\mathrm{exo}}) = (2.5 \pm 1.0) \times 10^{10}\,\mathrm{m}^{-3}$ for Mariner 7. Thus, the values derived with our exosphere model agree with the ones published by Anderson and Hord (1971) within a factor of 2. The error bars of the Mariner values are notably smaller because the Mariner measurements were obtained with a UV spectrometer that was designed for this task. Since our interpretation of the Mariner measurements is consistent with the one published 35 years ago by Anderson and Hord (1971) we conclude that the values derived from UV airglow measurements do not critically depend on the specific exosphere model.

TABLE I

Overview of fit results. The three upper lines refer to the single-component approach (see Equations (20) to (25)), whereas for the three lower rows we have assumed the co-existence of a cool and a hot hydrogen component. The temperature T_{cool} is not a fit value, it has been taken from Lichtenegger *et al*. (this issue).

Dataset	T_{hot} (K)	$n_{\mathrm{H,\,hot}}$ (m^{-3})	T_{cool} (K)	Maximum $n_{\mathrm{H,cool}}$ (m^{-3})
Mars Express	$1000\,^{+\infty}_{-400}$	$6.4\,^{+4.0}_{-0.6} \times 10^{9}$	–	–
Mariner 6	$350\,^{+100}_{-50}$	$7.1\,^{+0.7}_{-1.6} \times 10^{10}$	–	–
Mariner 7	425 ± 50	$3.4\,^{+1.6}_{-0.5} \times 10^{10}$	–	–
Mars Express	1000	6×10^{9}	180	$<1.2 \times 10^{10}$
Mariner 6	350	6.3×10^{10}	210	$<4.2 \times 10^{10}$
Mariner 7	425	3.1×10^{10}	210	$<3.4 \times 10^{10}$

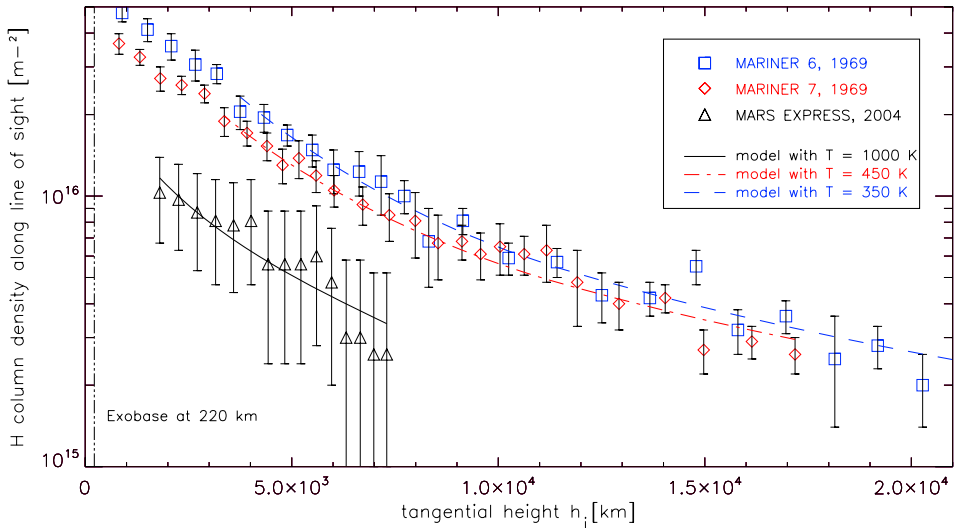

Figure 9. Measured column densities of neutral hydrogen (symbols) plotted against tangential height h_i. The solid lines represent models with values for the temperature and for the exobase density (denoted in Equation (20) to (25)) that minimize the χ^2-statistics. The most notable difference between the NPD measurements from 2004 (triangles) and the Mariner 6 (rectangles) and Mariner 7 (diamonds) data is the diminished exosphere density.

Generally, the upper exosphere in 2004 appears to be much thinner and hotter than in 1969. Note that we took into account the different solar irradiance, which was only 25% higher in 1969, and obviously falls short of explaining the 5 times higher hydrogen density during the Mariner mission compared to the Mars Express measurement. One reason why NPD measured lower UV fluxes might be the different observation geometry: The Mariner measurements were made from above the sun-illuminated Mars surface at solar zenith angles of 27° and 44°, whereas the NPD measurement was made from above the nightside at a solar zenith angle of 145° (see Figure 1). The exobase is expected to show a large spatial variability that results in an asymmetric exosphere. The model of Holmström (this issue) predicts a spatial variability of the exobase density of up to one order of magnitude. The North pole region where the NPD observation was made shows the lowest exospheric densities (Holmström, this issue). There are, however, other observations from spring 2004 where NPD measured the UV emission of the sun-illuminated Mars surface itself, which never exceeded 5 kR. From Mariner 9 measurements Barth *et al.* (1972) reported Lyman-α intensities from the Mars disk of up to 10 kR. This suggests that the Martian exosphere generally was thinner in 2004 than it was in 1969.

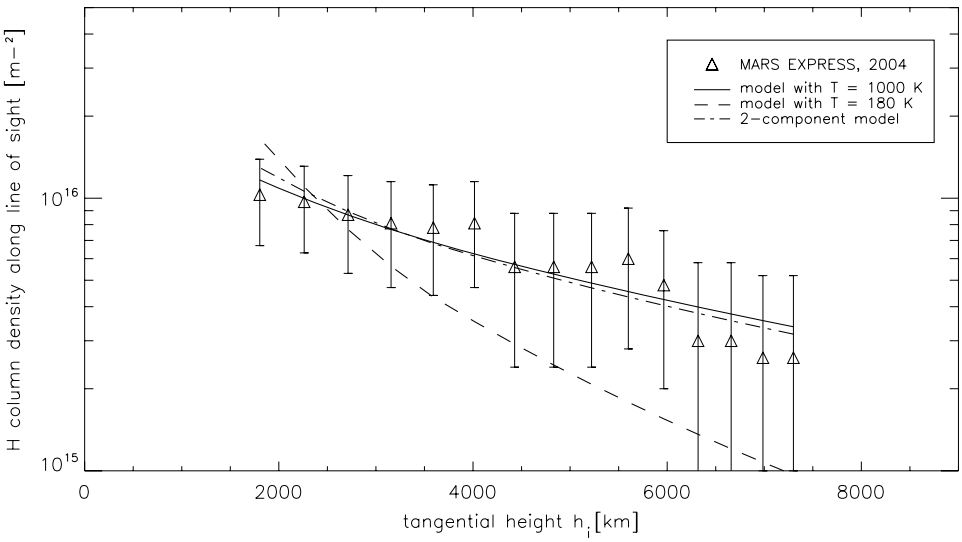

Figure 10. Example of a two-component model with very different temperatures that is still consistent with NPD data. The dashed-dotted line shows a density profile with $T_{\mathrm{cool}} = 180$ K, $T_{\mathrm{hot}} = 1000$ K, and with $n_{\mathrm{H,cool}}(r_{\mathrm{exo}}) = 1.2 \times 10^{10}\,\mathrm{m}^{-3}$, $n_{\mathrm{H,hot}}(r_{\mathrm{exo}}) = 6 \times 10^{9}\,\mathrm{m}^{-3}$.

6.2. Constraints on a Two-component Model

The temperatures derived in Section 6.1 for a one-component approach cannot be the bulk temperatures of the exosphere. The dominant CO_2 in the Martian atmosphere is a very efficient cooling agent (Lichtenegger *et al.*, 2002) and the aerobraking and mass spectrometry measurements at the exobase yield (see Lichtenegger *et al.* (this issue) for a summary) exospheric temperatures of only 150 to 230 K, for low and for high solar activity. The temperature of 350 K derived from Mariner measurements is considerably lower than the value found with the NPD data, but it is still significantly higher than the exospheric bulk temperature of ≤ 240 K that is derived from Mars Odyssey aerobraking data for a comparable solar activity (Lichtenegger *et al.*, this issue). To solve this paradoxon it is plausible to assume that several components of hydrogen co-exist in the Martian exosphere. If this approach is valid all UV airglow measurements have to be interpreted as a mixture of thermal (T close to the exobase bulk temperature of 150 to 230 K) atoms that are concentrated at the exobase and of hydrogen atoms with higher energies that have their origin in dissociative recombination and photodissociation processes. The Lyman-α airglow measurements are, of course, heavily influenced by the hottest component because the density of the cool component quickly drops with increasing altitudes. If we assume that our airglow measurements and those published by Anderson and Hord (1971) have given us correct estimates of the temperature of the hot component and that the temperature of the cool component is the one

obtained from aerobraking and mass spectrometry data at the exobase, we can test a simple two-component approach: We estimate the maximum exobase density of a cool component, which still would be in agreement with the three different UV limb emission profiles. If the exobase density of the cool component is much higher than the hot component this influences notably the limb emission profile even at altitudes that fall within our airglow observation range. For this analysis we have set $T_{\mathrm{cool}} = 180$ K for 2004 (solar minimum conditions) and $T_{\mathrm{cool}} = 210$ K for 1969 (solar maximum conditions) according to Lichtenegger *et al.* (this issue). T_{hot} is assumed to be the temperature fitted for the single component model (see Equations (20), (22), (24)). The results of this analysis are given in Table I in the three lower rows, Figure 10 illustrates the two-component approach for the NPD measuremet.

7. Conclusion

Although the NPD sensor was not designed as UV detector, the Lyman-α airglow measurements done by the Mariner 6 and 7 missions (Anderson and Hord, 1971; Barth *et al.*, 1971) have been reproduced successfully. We have fitted a model density profile of exospheric hydrogen to UV limb emission measurements done in 2004 during low solar activity, the height ranging from 1,900 to 7,250 km. In the case of a single hydrogen component our model allows for a well constrained value of the exobase density of $n_{\mathrm{H}}(r)_{\mathrm{exo}} = 6.4 \times 10^9$ m^{-3}. However, the optimum temperature of $T = 1000$ K is poorly constrained because of the statistical errors and because the modeled density profile shows no strong variation for temperatures much higher than 1000 K. In 2004 at low solar activity the hydrogen exosphere appeared to be thinner and hotter than in 1969 at high solar activity. The variability of the upper Mars exosphere is generally high. In 1969 the exobase density decreased by a factor of 2 (see Table I) within one single week, the solar zenith angles being similar. In 2004 the exosphere seems thinner by a factor of 5 than in 1969. The different observation direction or the spatial variability might explain this discrepancy; the minimum surface density for April 2004 is predicted (Holmström, this issue) for the region above the North pole where the NPD observation was made. Unfortunately, we do not have other limb emission measurements from NPD to track the spatial or temporal variability of the exosphere.

If there are several components of exospheric hydrogen with different scale heights the exosphere parameters we have inferred from the measurements are dominated by the hotter components. The Mariner data from 1969 seem to rule out the presence of a cool ($T = 210$ K) hydrogen component that is much denser than the observed hot one (see Table I); the temperature estimate does not increase if one restricts the evaluation step by step to the data points obtained at higher altitudes. Thus, the Mariner data on their own give no motivation to adopt a multi-component approach. Nonetheless, a two-component model with an average temperature of about 250 K and a total exobase density of 10^{11} m^{-3} hydrogen atoms may fit the

Mariner data as well as a one-component model. The NPD measurement in 2004 does not rule out the presence of a cool component with an exobase density higher than the observed hot component: A two-component exosphere model with a cool (180 K) and a hot (600 K) component with an average temperature of only 320 K would still be consistent with the NPD measurements. The hydrogen exobase temperatures that are derived from UV airglow measurements generally depend on the number of components one assumes, the derived temperature is bound to be dominated by the hotter components and should therefore not be used as an estimate for the exobase bulk temperature. Lichtenegger *et al.* (this issue) show that all temperature estimates for the Martian exosphere that were derived from Lyman-α airglow observations are significantly higher than the values derived from mass spectrometry and aerobraking measurements, which are sensitive around the exobase. The hydrogen exobase density is better constrained by our UV airglow measurement: Even if we allow for a cool hydrogen component our data rule out exobase densities above 2×10^{10} m^{-3} in 2004 above the North polar region.

Beside the Mariner 6 and 7 missions, there was only one Lyman-α airglow measurement at high altitudes before the arrival of Mars Express. In 1972, for medium solar activity (solar activity index of 70, $F_{10.7} = 120$), Dementyeva *et al.* (1972) found a hydrogen exobase density of only $n_{\mathrm{H}}(r)_{\mathrm{exo}} = 6 \times 10^9$ m^{-3}. They did, however, not calculate an optimal fit temperature; they assumed that $T = 350$ K, derived from Mariner 6 and 7 data, also applied to their observation (for an overview of temperatures derived for the martian exosphere over the last 35 years refer to Lichtenegger *et al.*, this issue, Figure 4a). Preliminary results from Lyman-α airglow data obtained with the SPICAM UV spectrograph on Mars Express (Chaufray *et al.*, 2006) yield exobase densities of a few to several 10^{10} m^{-3} above the dayside. For some observation configurations the emission profile requires two different hydrogen components with $T_{\mathrm{hot}} > 600$ and $T_{\mathrm{cool}} = 200$ K. The average exospheric temperature appears to be higher than 340 K (Chaufray *et al.*, 2006). The basic problem with comparing Lyman-α airglow data to each other may be that the exosphere is highly variable for different locations.

Although the accuracy of the NPD data is poorer than those measured by Mariner 6 and 7 it can be seen that the Mars exosphere above the North pole region was thinner and hotter for low solar activity than in 1969 at solar maximum. Preliminary results of Lyman-α airglow measurements done with SPICAM above the dayside yield exobase densities similar to the Mariner 6 and 7 data (Chaufray *et al.*, 2006). In any case we do not see (including the work of Dementyeva *et al.* (1972)) a trend to higher exobase densities for low solar activity, which was predicted by the exospheric models of Krasnopolsky and Gladstone (1996) and of Krasnopolsky (2002). If the Lyman-α data are interpreted as measurements of an energetic hydrogen population that is considerably hotter than the hydrogen bulk temperature, lower exospheric densities for low solar activity seem intuitive. In 2004 the solar activity was lower, the photodissociation rates were lower and thus the component of energetic hydrogen was less pronounced than in 1969. Krasnopolsky and

Gladstone (1996) use the Mariner measurements as input for the one-component hydrogen exosphere in their model and assume an extreme sensitivity to the solar cycle. Their model predicts for solar minimum conditions an exobase hydrogen density of $n_H = 10^{12}$ m^{-3} and $T = 200$ K. Models on atmospheric loss and on ENA production (see for instance (Barabash *et al.*, 2002; Holmström *et al.*, 2002; Lichtenegger *et al.*, 2002)) that use the values given by Krasnopolsky and Gladstone (1996) therefore have to be revised since their predictions critically depend upon the exosphere density and temperature. A more recent model of Krasnopolsky (2002) yields somewhat lower densities ($n_H = 2 \times 10^{11}$ m^{-3} for a solar activity index of 42), but these are still more than one order of magnitude away from our NPD observation.

The NPD measurement presented in this work is not the only experimental evidence that the Martian hydrogen exosphere is considerably thinner than previously modeled for low solar activity. We have already mentioned the Lyman-α airglow measurements done with SPICAM, but there are also non-photometric evidences: With NPD we also have mapped the outflow of hydrogen and oxygen ENAs from Mars (Galli *et al.*, this issue). We have found that the outflow is at least one order of magnitude below theoretical predictions that relied on the exosphere model of Krasnopolsky and Gladstone (1996). The detected H-ENA and O-ENA intensities are consistent with model predictions only if a thin neutral exosphere with hydrogen column densities of 10^{16} m^{-2} along the NPD line-of-sight is assumed. This is the value we also have found in this work based on the Lyman-α airglow (Figure 8).

Based on Mariner and NPD data we tentatively advise modelers to use a few 10^{10} m^{-3} as the spatially averaged exobase density for hydrogen, for low and for high solar activity. The expected spatial variability of the exosphere (Holmström, this issue) may be too notable to be neglected; many models on ENA and ion production have implied a constant exobase density and temperature over the entire planet.

The basic physical properties of the Martian exosphere obviously are not well known yet. There are clear disagreements between theoretical models and data and between different types of measurements. More measurements at the exobase are needed to understand the photochemistry and the heating mechanisms in the Martian atmosphere. The UV airglow measurements are only an indirect way of measuring the temperature and the density of the exosphere. The present situation could be comparable with the investigation of the Venusian exosphere some decades ago. The temperature of the hydrogen exosphere on Venus was also overestimated because the UV airglow measurements were dominated by hot hydrogen atoms far above the exobase. After the first direct mass spectrometer data the estimate of the exospheric temperature had to be reduced from 700 K down to 300 K (Lichtenegger *et al.*, this issue). It remains, however, to be shown why the hot hydrogen component has an exobase density that is comparable to the one of the cool component at Mars, whereas at Venus the exobase density of the cool component is 100 times higher (Bertaux *et al.*, 1978) than the hot one. A more accurate picture of the Mars exosphere will hopefully be gained one day from direct mass spectrometer data.

References

Anderson, D. E., and Hord, C. W.: 1971, *JGR* **76**(28), 6666.

Anderson, D. E.: 1976, *JGR* **81**(7), 1213.

Barabash, S., Holmström, M., Lukyanov, A., and Kallio, E.: 2002, *JGR* **107**(A10), 1280.

Barabash, S., *et al*.: 2004, ASPERA-3: analyser of space plasmas and energetic ions for Mars Express, 2004mesp.book, 121.

Barth, C. A., Hord, C. W., Pearce, J. B., Kelly, K. K., Anderson, G. P., and Stewart, A. I.: 1971, *JGR* **76**(10), 2213.

Barth, C. A., Stewart, A. I., and Hord, C. W.: 1972, *Icarus* **17**, 457.

Bertaux, J. L.: 1978, *PSS* **26**, 431.

Bertaux, J. L., Blamont, J., Marcelin, M., Kurt, V. G., Romanova, N. N., and Smirnov, A. S.: 1978, *PSS* **26**, 817.

Bougher, S. W., Engel, S., Roble, R. G., and Foster, B.: 2000, *JGR* **105**(E7), 17669.

Chaufray, J. Y., Quémerais, E., Bertaux, J. L., and Leblanc, F.: 2006, Sounding of the martian upper atmosphere with SPICAM on Mars Express, Europlanet conference 2006, abstract Nr. 00566.

Chamberlain, J. W.: 1963, *PSS* **11**, 901.

Dementyeva, N. N., Kurt, V. G., Smirnov, A. S., Titarchuk, L. G., and Chuvahin, S. D.: 1972, *Icarus* **17**, 475.

Deutscher, S. A., Borisov, A. G., and Sidis, V.: 1999, *Phys. Rev. A* **59**(6), 4446.

Emerich, C., Lemaire, P., Vial, J.-C., Curdt, W., Schühle, U., and Wilhelm, K.: 2005, *Icarus* **178**, 429.

Galli, A., Wurz, P., Barabash, S., Grigoriev, A., Gunell, H., Lundin, R., *et al*.: this issue, Space Sci. Rev., doi: 10.1007/s11214-006-9088-8.

Holmström, M., Barabash, S., and Kallio, E.: 2002, *JGR* **107**(A10), 1277.

Holmström, M.: this issue, Space Sci. Rev., doi: 10.1007/s11214-006-9036-7.

Krasnopolsky, V. A., and Gladstone, G. R.: 1996, *JGR* **101**(A7), 15765.

Krasnopolsky, V. A.: 2002, *JGR* **107**(E12), 5128.

Krasnopolsky, V. A., and Gladstone, G. R.: 2005, *Icarus* **176**, 395.

Lammer, H., Lichtenegger, H. I. M., Kolb, C., Ribas, I., Guinan, E. F., Abart, R., *et al*.: 2003, *Icarus* **165**, 9.

Leblanc, F., Chaufray, J. Y., Lilensten, J., Witasse, and Bertaux, J.-L.: 2006, *JGR* **111**(E9), 11.

Leinert, C., *et al*.: 1998, *A&A Sup. Ser.* **127**, 1.

Lichtenegger, H. I. M., Lammer, H., and Stumptner, W.: 2002, *JGR* **107**(A10), 1279.

Lichtenegger, H. I. M., Lammer, H., Kulikov, Yu. N., Kazeminejad, S., Molina-Cuberos, G. H., Rodrigo, R. *et al*.: this issue, Space Sci. Rev., doi: 10.1007/s11214-006-9082-1.

Lundin, R., Zakharov, A., Pellinen, R., Borg, H., Hultqvist, B., Pissarenko, N., *et al*.: 1989, *Nature* **341**, 609.

Meier, R. R.: 1991, *SSR* **58**, 1.

NASA: 2004, The Solar Radiation and Climate (SORCE) Experiment, http://lasp.colorado.edu/-sorce/sorce_data_access.

NASA: 2006, The Solar Wind Anisotropies (SWAN) experiment, http://sohowww.nascom.nasa.-gov/gallery/SWAN/index.html.

Nier, A. O., and McElroy, M. B.: 1977, *JGR* **82**(28), 4341.

Thomas, G. E.: 1963, *JGR* **68**(9), 2639.

Wurz, P., and Lammer, H.: 2003, *Icarus* **164**, 1.